Title
Acoustic Predictions for the Side-by-Side Air Taxi Rotor in Hover

Journal
Proceedings of the Vertical Flight Society 77th Annual Forum and Technology Display

Authors
Sagaga, Jared
Lee, Seongkyu

Publication Date
2021-05-10

DOI
10.4050/f-0077-2021-16695

Acoustic Predictions for the Side-by-Side Air Taxi Rotor in Hover

Jared Sagaga
Ph.D. Student

Seongkyu Lee
Associate Professor

Department of Mechanical and Aerospace Engineering
University of California, Davis
Davis, California, 95616 U.S.A.

ABSTRACT

In this paper, acoustic predictions are performed for the rotors of NASA's side-by-side Urban Air Mobility (UAM) aircraft in hover. Investigations of the acoustics are performed on four overlap configurations, 0%, 5%, 15%, and 25%, in hover via high-fidelity Computational Fluid Dynamics (CFD) simulations. CFD simulations are carried out using the HPCMP CREATE™-AV Helios and acoustics calculations are conducted using PSU-WOPWOP. Blade airloads and performance of the rotors are computed for this study. Predictions on the rotor airloads and wake geometry are compared for all overlap configurations at a collective pitch angle of 8°. It is shown that the 25% overlap configuration yields a higher overall sound pressure level (OASPL) than for the other overlap configurations, mainly due to stronger blade-vortex-interactions at the entrance and exit locations of the overlap region. It is found that the OASPL difference in hover is above 62 dB at an altitude of 500 ft (152.4 m), which is the UAM aircraft noise guideline suggested by Uber. Additionally, noise for all overlap cases are compared against various background noise levels. Results show that noise from the side-by-side rotor could not be fully concealed by the various background noise at an altitude of 500 ft (152.4 m).

NOMENCLATURE

R	rotor radius, m
N_b	number of blades
c_{ref}	blade reference chord, m
c	speed of sound in the undisturbed medium, m/s
C_{tip}	tip chord length, m
F_z	blade normal force, N/m
dF_z	blade sectional normal force, N/m
$dF_z/d\Psi$	azimuthal derivative of sectional normal force, N/m
$\vec{l}$	blade surface loading vector, N/m
l_r	$\vec{l}\cdot\hat{r}$, N/m
M_r	$\vec{M}\cdot\hat{r}$
M_∞	freestream Mach number
r/R	nondimensional radial position
r	distance between $\vec{y}$ and $\vec{x}$, m
p'	total acoustic pressure, Pa
p'_L	loading noise acoustic pressure, Pa
p'_T	thickness noise acoustic pressure, Pa
q	q-criterion, $\frac{1}{2}(\|\|W_{ij}\|\|^2 - \|\|S_{ij}\|\|^2)$, 1/s^2
$\bar{q}$	non-scaled q-criterion, $q/(c_\infty/L_{ref})^2$
S_{ij}	strain-rate tensor, 1/s^2
t	observer time, s
$\triangle s$	grid spacing, m
W_{ij}	spin-rate tensor, 1/s^2
$\vec{x}$	observer location, m
$\vec{y}$	acoustic source location, m
θ_o	blade collective pitch, deg
ρ_o	air density, kg/m^3
v	local fluid velocity on the blade surface, m/s
Ψ	rotor azimuth, deg

Acronyms

CFD	Computational Fluid Dynamics
CCW	counterclockwise
CW	clockwise
VTOL	vertical take-off and landing
SPL	sound pressure level, dB
OASPL	overall sound pressure level, dB
UAM	Urban Air Mobility
VTOL	vertical take-off and landing

INTRODUCTION

Multi-rotor air vehicles or Vertical Take-Off and Landing (VTOL) aircraft have gained a lot of interest over the last several years with a great potential to support the concept of Urban Air Mobility (UAM) (Refs. 1–3). One of the main goals of UAM is to deliver packages, which is already en route with retail industry. However, an even more ambitious goal of UAM is to provide public transportation that is environmentally friendly, safe, and affordable to urban residents. This is all in response to increasing urbanization, crowding and congestion on roads making ground transport

Presented at the Vertical Flight Society 77th Annual Forum & Technology Display, Virtual Event, May 11–13, 2021.

increasingly difficult to operate effectively within urban environments. The current ground transportation services are currently experiencing tremendous strain even more in densely populated cities. Electric VTOLs (eVTOL) or hybrid-electric VTOLs, are two types of UAM air vehicles that can provide solutions to alleviate that strain on existing city networks. There are also other essential applications that can benefit from UAM including transporting of goods for medical purposes. With a wide range of applications, an initiative for UAM presents possible and viable solutions to moving both people and goods in urban areas. However, there are barriers for this platform to be successful. For example, noise and public acceptance will be critical to the success of UAM. Uber recommended (Ref. 4) that the UAM aircraft noise should be 62 dB at 500 ft altitude or 67 dBA at 250 ft altitude.

The design space for UAM VTOL is wide-ranging and there is much more that remains to be explored in this area, as opposed to conventional helicopters, which have only a main rotor and a tail rotor. Typical UAM VTOL aircraft designs have multiple rotors (mostly electric or hybrid) with a smaller rotor radius in distributed propulsion as shown in Fig. 1. UAM VTOL designs may also have a higher rotation rate compared to conventional rotorcraft, as well as possibly the addition of lifting wing surfaces much like compound helicopters. It is essential to account for multi-rotor interactional aerodynamics and acoustics for these UAM vehicle designs, compared to conventional helicopters. There are expectations of significant noise generation, tonal and broadband noise, due to complex aerodynamics interactions of multi-rotor UAM vehicles.

Fig. 1: A multi-rotor UAM vehicle from Airbus called the Vahana (Ref. 5)

A series of studies on conceptual design of UAM aircraft were performed by Johnson et al. (Refs. 3, 5, 6) for lift+cruise VTOL, quadrotor, and side-by-side rotor. There are also studies conducted by Ventura et al. (Refs. 7, 8) that includes high-fidelity CFD using OVERFLOW (Ref. 9) loosely coupled with a Computational Structural Dynamics (CSD) comprehensive analysis code, CAMRAD II, on NASA's six-passenger side-by-side hybrid (as seen in) VTOL configuration (rotors and fuselage) in forward flight. In this study, their results showed that the percentage of the overlap region is a key parameter to the rotor airloads and cruise performance. They also found that results from the 15% overlap configuration yielded the best lift-to-drag ratio.

Jia and Lee (Refs. 10–12) investigated NASA's quadrotor and side-by-side rotor concept design studies, not only predicting the aerodynamic performance, but also performing the acoustic predictions in forward flight condition. Their results showed that blade vortex interaction (BVI) events, generate significant noise. For example, the side-by-side rotor study, the increasing the overlap region significantly enhanced rotor-to-rotor BVI noise. They also conducted a study the effect of the finest grid spacing (5% C_{tip} and 10% C_{tip}) in the refinement off-body region on the aerodynamic and acoustic predictions, and they found that 10% C_{tip} is sufficient to capture BVI noise. These early studies on different UAM aircraft noise were conducted only for forward flight conditions. However, noise could also be significant in hover, which is especially important for UAM operations due to the close proximity to the ground personnel. Sagaga and Lee (Ref. 13) studied the hover performance for the side-by-side rotor configuration with various values of the overlap.

Fig. 2: Six-passenger side-by-side air taxi VTOL concept design from NASA (Ref. 5)

The objective of this work is use a first-principles and high-fidelity CFD method to perform an analysis on the acoustics of NASA's six passenger side-by-side UAM vehicle in the hover condition. From the results of the high-fidelity CFD, possible sources of noise can be identified including blade-vortex-interactions. We present the effect of the rotor-to-rotor overlap percentage on the strength of the noise being generated as well as on the far-field noise directivity. Noise generated from the aerodynamic interactions of the side-by-side rotors due to overlap is compared to that from an isolated rotor (hover condition) as well as to background noise. Ultimately, this paper is to assess the viability of UAM operations in urban areas at low altitudes.

METHODOLOGY

First-principles unsteady and compressible Navier-Stokes equations are solved to capture unsteady flow, radial flow, swirl flow, compressibility, flow separation, and blade-vortex interaction for the rotors of the six-passenger side-by-side hybrid VTOL UAM configuration as shown in Fig. 2 (Ref. 5). CFD calculations are performed using CREATE^{TM}-AV Helios (Ref. 14) using the OVERFLOW module in the near-body and SAMCart in the off-body. For the off-body mesh, it uses a fine structured mesh with an adaptive Cartesian mesh refinement to aide in resolving the tip vortices. Simulations in the present work will only include the left (CW) and right (CCW) rotors without the fuselage. There is a 45° phase shift applied to the left rotor as seen in Fig. 3. Different overlapping cases, including 0%, 5%, 15%, and 25%, are considered in order to investigate the effect of the overlap distance between the left and right rotors on acoustics. For each overlap case, the amount of distance between two rotors direction defines the percentage in the overlap region. These overlap distances are nondimensionalized using the radius (R) of the rotor. The separation distances between the left and right rotor centers for 0%, 5%, 15%, and 25% overlap correspond to $2R$, $1.9R$, $1.7R$, and $1.5R$. Since the material properties are not made available from the initial design phase of the vehicle, the rotor blades are modeled as rigid (no elastic deformation). Other vehicle's design parameters are presented in Table 2. Details on the CFD solver, grids, and settings are outlined in the subsequent sections. The Boeing VR-12 and Sikorsky SSC-A09, two modern airfoils are used for the rotor blades. Along the span at $R < 85\%$, the VR-12 is used, and at $R > 95\%$, the SSC-A09 is used. In the 85% and 95% spanwise locations, a linear interpolation between the SSC-A09 and VR-12 is assumed. Both the blade chord and twist distributions are assumed linear. Between the $R = 0.94\%$ and blade tip, there is a 15° linear swept-tapered ratio, which can be seen in Fig. 4, depicting the blade planform.

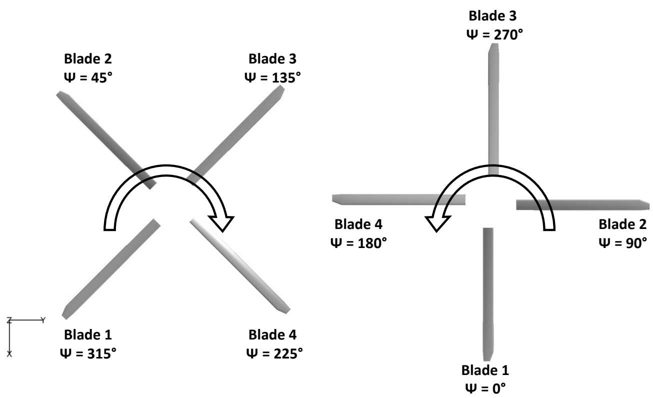

Fig. 3: Side-by-side rotor configuration with no overlap

Table 1: Basic properties for the side-by-side air taxi

Rotors	2
Blades per Rotor	4
Rotor Radius	10.5 ft (3.2 m)
Tip Chord Length	0.43 ft (0.13 m)
Nominal Rotor Speed	499.97 RPM
Nominal Rotor Tip Speed	621.7 ft/s (189.5 m/s)
Gross Weight	3,950 lb (1,792 kg)

CFD Simulation Setup

OVERFLOW, a high-fidelity and overset structured flow solver developed and maintained by NASA, is used as the near-body solver in Helios. An off-body Cartesian solver, SAMCart, in conjunction with AMR is used to capture the rotor wakes and tip vortices shedding off. In OVERFLOW, we apply a fifth-order central difference spatial scheme for the inviscid terms. With the viscous terms, a second-order discretization scheme is used. For temporal discretization,

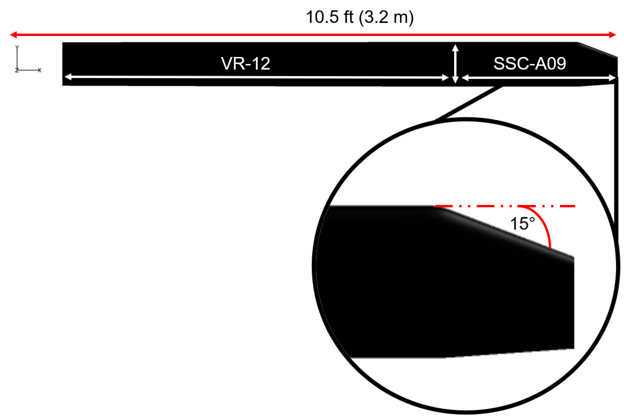

Fig. 4: Rotor blade planform

a second-order diagonalized Beam Warming pentadiagonal scheme is used along with dual-time stepping subiterations. The Spalart-Allmaras DES option is used in the near-body in order to resolve viscous turbulent flows near the wall and to resolve the wake in the off-body. A rotation curvature correction model is used. Time-accurate simulations for the present work are divided into two different time-step simulations to reduce computational time. In the initial run, time-step size is set to 1.0° azimuth for 2,880 timesteps or 8 rotor revolutions. A restart is then initiated for the second run, for which we switch to a finer time-step size of 0.25° azimuth for 5,760 timesteps or 4 rotor revolutions. All CFD simulations were carried out on the Centennial (SGI-ICE-XA) or Excalibur (Cray XC40) high performance computer (HPC) located at the U.S. Army Research Laboratory and U.S. Department of Defense (DoD) Supercomputing Resource Center (DSRC). A total of 20 nodes (800 cores) on Centennial or 25 nodes (800 cores) on Excalibur were used for all simulations. Table 2 and Table 3 respectively shows the simulation settings and presents the breakdown of the computational cost for each simulation.

Table 2: Simulation settings | All overlap cases

Near-body settings	
Grid type	Structured grid
Spatial scheme	fifth-order accurate
Turbulence model	SA-DES
Off-body settings	
Grid type	Cartesian AMR
Finest wake-grid spacing	10% C_{tip} spacing
Spatial scheme	Fifth-order accurate
Turbulence model	SA-DES

CFD Grids

A dual-mesh paradigm is employed in Helios, as mentioned earlier, which divides the entire computational domain into the near-body (structured/unstructured) and off-body (structured) mesh systems. The rotor blades are modeled using

Table 3: Computational size and cost | All overlap cases

Near-body grid	
Per rotor blade	4.9 million
Both rotors	39.2 million
Off-body grid	
AMR OFF	153.5 million
AMR ON	625.9 million
Number of processors	800
Simulation time per rotor revolution (hrs)	2.5 | First 8 revs 19 | Last 4 revs

an overset structured mesh for the near-body with an O-grid topology, and the far-field is modeled in the off-body using an adaptive Cartesian grid. The near-body mesh was created using NASA's Chimera Grid Tools (CGT), which is an overset grid generation software. As shown in Fig. 5, the surface mesh of the blade is closely inspected at the blade root and tip. As for the details on grid resolution, there are 265 points around the airfoil, 165 points in the spanwise direction, and 65 points in the normal direction. The spacings at the leading and trailing edges are set to 0.05% C_{tip} and 0.02% C_{tip}, respectively, with C_{tip} being the tip chord of the blade. The spacing at wall of 1.0×10^{-5} meters, in order to achieve a y+ (dimensionless wall distance) of 1.0.

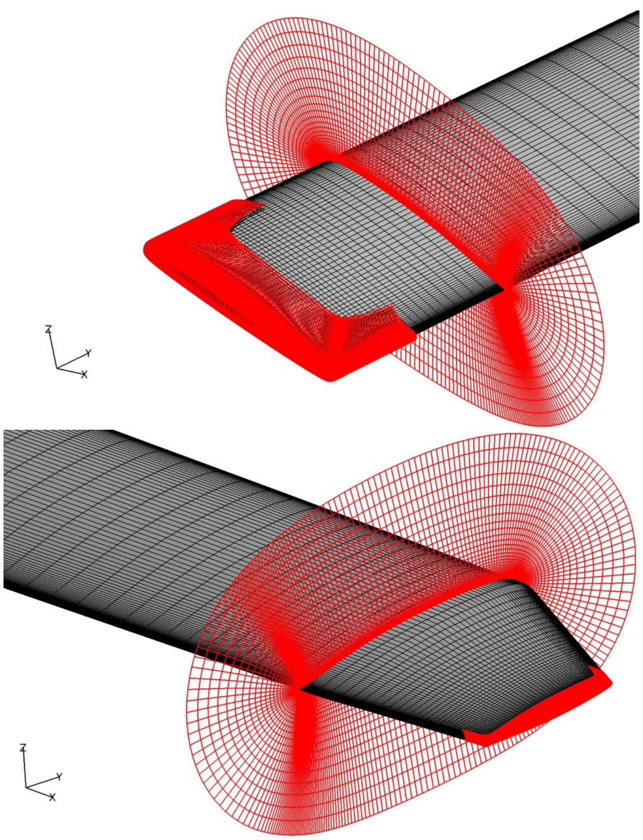

Fig. 5: Near-body grids at the blade root (Top) and blade tip (Bottom)

In the near-body volume grids, the end spacing is set to 10% C_{tip}. For the off-body Cartesian volume grids, the finest spacing is set to 10% of the C_{tip}. The number of points for each rotor blade is approximately 4.9 million, and a total of 39.2 million grid points are used for all eight rotor blades.

The Cartesian grid in the off-body is automatically generated by SAMCart using eight refinement levels with an adaptive mesh refinement (AMR) turned on after eight rotor revolutions. AMR is a feature in SAMCart, which helps capture the detailed physics of the rotor wakes including any and all shedding tip vortices within the defined AMR region as seen in Fig. 7. There is a fixed refinement box surrounding the two rotors, which is used to resolve and capture the flow physics and wake near the rotor blades. The spacing in the fixed refinement box is set to be 10% C_{tip}, which matches the spacing on the outer-boundary of the near-body volume grids, and its spacing does not change throughout the duration of the simulations as opposed to the AMR region. Setting a fixed refinement box with an adaptive region for tracking the shedding vortices especially in the far-wake can also help reduce the cost for these types of simulation cases. The size of the refinement box is set to $1.25R$ in the x-direction, $2.5R$ in the y-direction, $0.25R$ in the positive z-direction, and $2R$ in the negative z-direction as seen in Figs. 6 and 7. The total number of grid points in the off-body grid is approximately 800 million grid points after 12 rotor revolutions. The domain size for the off-body is set to 20 rotor radii away from the origin in every direction.

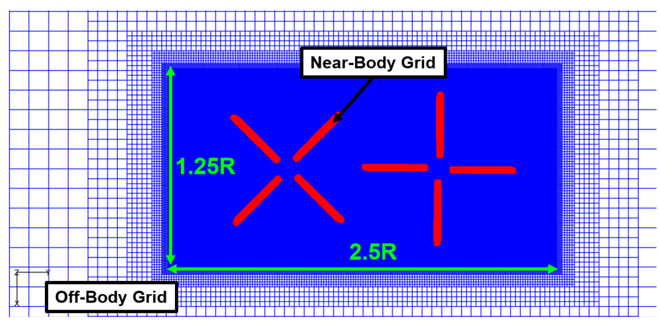

Fig. 6: Off-body grid (Top view)

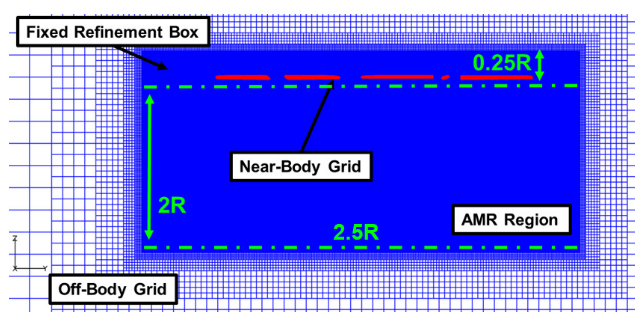

Fig. 7: Off-body grid (Side view)

Acoustic Simulation Setup

An acoustic prediction tool, PSU-WOPWOP (Refs. 15, 16), is used for the acoustic predictions in this work. Farassat's Formulation 1A (Refs. 17, 18) of the Ffowcs Williams and Hawkings (FW-H) equation (Ref. 19) is numerically implemented in PSU-WOPWOP. The Formulation 1A from Farassat is determined on the impermeable surface approach used in the present work. As seen below are the equations for the Farassat Formulation 1A:

$$p'(\vec{x},t) = p'_T(\vec{x},t) + p'_L(\vec{x},t) \tag{1}$$

$$\begin{aligned} 4\pi p'_T(\vec{x},t) = & \int_{f=0} \left[\frac{\rho_\infty (\dot{v}_n + v_{\dot{n}})}{r|1-M_r|^2} \right]_{ret} dS \\ & + \int_{f=0} \left[\frac{\rho_\infty v_n \left(r\dot{M}_r + c(M_r - M^2) \right))}{r|1-M_r|^3} \right]_{ret} dS \end{aligned} \tag{2}$$

$$\begin{aligned} 4\pi p'_L(\vec{x},t) = & \frac{1}{c_\infty} \int_{f=0} \left[\frac{\dot{l}_r}{r|1-M_r|^2} \right]_{ret} dS \\ & + \int_{f=0} \left[\frac{l_r + l_M}{r^2|1-M_r|^2} \right]_{ret} dS \\ & + \frac{1}{c_\infty} \int_{f=0} \left[\frac{l_r(r\dot{M}_r + c(M_r + M^2))}{r^2|1-M_r|^3} \right]_{ret} dS \end{aligned} \tag{3}$$

In the equations above, p' denotes the total acoustic pressure, p'_T denotes the thickness acoustic pressure, which is induced by the motion of the blade, and P'_L denotes the loading noise acoustic pressure, which is generated by lift and drag of the rotating blades. ρ_o is the fluid density, c is the speed of sound, r is the distance of the source's position ($\tilde{y}$) to the position ($\tilde{x}$) of the observer, v_n is the blade velocity in the normal direction, l_r is a component of the blade loading of the surface in the radiation direction, $\dot{l}_r$ denotes the change in the blade loading of the surface with respect to the change in the acoustic source/retarded time, and M_r is the Mach number of the blade surface in the radiation direction toward the observer's location. The integrands of Farassat's Formulation 1A are evaluated at the retarded time as denoted by *ret* in the above equations.

It is also important to note the two terms that have a significant influence on the magnitude of the acoustic pressure in Farassat's Formulation 1A. These terms are the:

1. Doppler amplification factor, $\frac{1}{|1-M_r|}$.
2. The sudden change within the airloads with respect to the retarded time, $\dot{l}_r$.

In particular, the second term is important for BVI noise since this term becomes large at the onset of BVI events.

In the acoustic simulations performed, a single observer is positioned at the 90° elevation angle, 500 ft (152.4 m) below the rotor disk plane in order to assess Uber's noise guidelines. An representation of the single observer grid can be seen in Fig. 8.

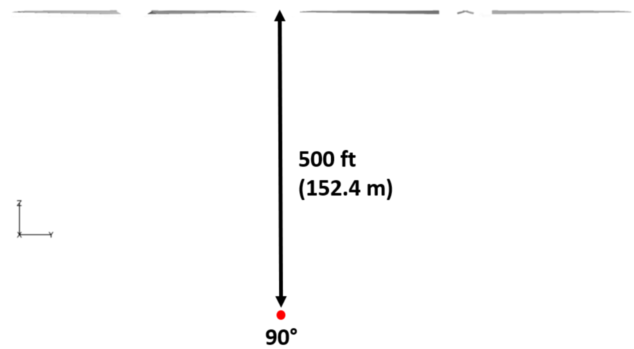

Fig. 8: Single observer location (not to scale | side view)

RESULTS

The side-by-side rotor configuration of NASA's urban air taxi concept is simulated in the hover condition using Helios (V8.1). All overlapping configurations of the side-by-side rotors, 0%, 5%, 15%, and 25%, are simulated with a collective pitch angle of 8°. In a previous study (Ref. 13), the aerodynamics of the side-by-side rotors were investigated including 24 simulations with a range of collective pitch angles from 4° to 12° in increments of 2°. After 12 rotor revolutions, all forces and moments of each CFD simulation case were found to be fully converged, with a total of 8,640 timesteps.

Effect of Rotor Overlap on Flow Fields and Airloads

In Fig. 9, it shows a comparison for all the overlap configurations for the iso-surfaces of a non-scaled q-criterion and colored by the vorticity magnitude at the last timestep where the forces and moments are converged. It is interesting to find that in Fig. 9, self-BVI events can be seen on each rotor in all the overlap cases. However, in the 5%, 15%, and 25% overlap cases, there are also rotor-to-rotor BVIs, indicating that there are aerodynamic interactions between the tip vortex of one rotor and the blade surface of the other rotor. The interaction between the tip vortex with the blade causes the large peaks in the total acoustic pressure for all overlap configurations.

Figure 10 (a) shows the entrance and exit of the overlap region at the 25% overlap case. The tip vortices are not clearly visible within the overlap region since they are rapidly convected to the downstream due to high induced velocities in the overlap region as shown in Fig. 11. Also, in Fig. 10 (b), a formation of an Omega shaped vortex structure is shown as a result from a merge of the two tip vortices from each rotor when they enter and exit the overlap region. There are also smaller secondary worm-like structures moving upwards in the +Z direction as seen in Fig. 10 (c), and these structures are pulled by the circulation of the tip vortices. These small secondary worm-like structures were investigated in previous studies for isolated rotor cases (Refs. 20–23), in which the grid resolution and sub-iteration convergence were studied on how each affects the formation of these secondary structures.

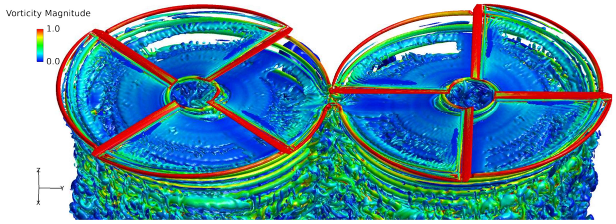

(a)

0% Overlap

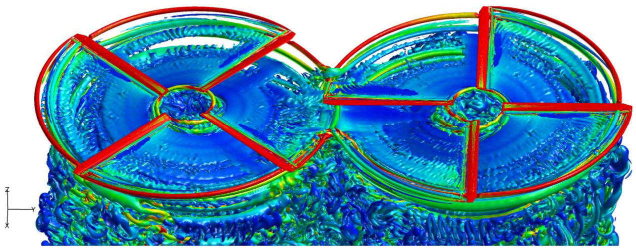

(b) 5% Overlap

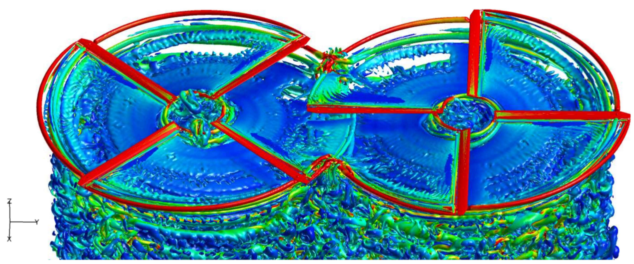

(c) 15% Overlap

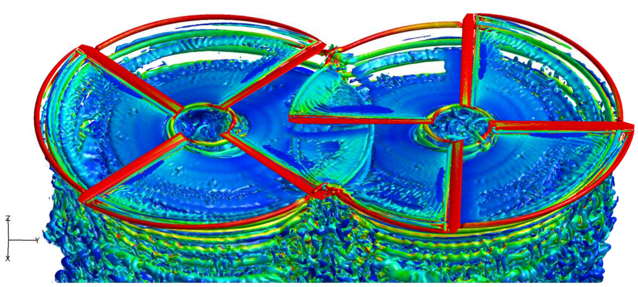

(d) 25% Overlap

Fig. 9: Isometric view of the iso-surfaces of a non-scaled q-criterion for all the overlap cases, colored by vorticity magnitude.

In Fig. 11, it shows a comparison of the induced inflow ratio for all the rotor overlap configurations. It can be seen that the induced inflow ratio increases significantly as the overlap region increases. The increased induced inflow ratio is due to the overlapped tip vortex and wake effects from both rotors. Furthermore, the higher induced inflow ratio in the overlap region pushes the blade-tip vortices in the downward direction.

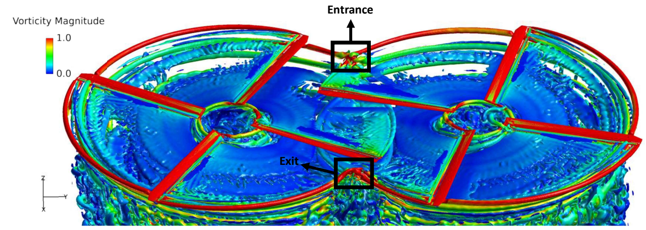

(a) Entrance and Exit locations

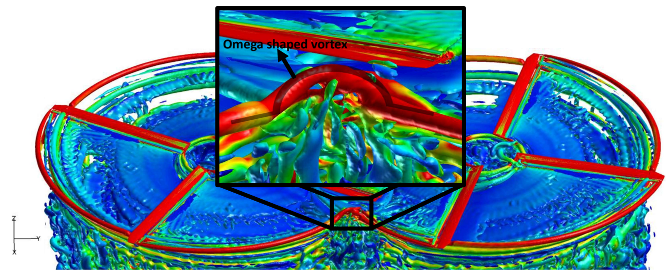

(b) Formation of Omega shaped vortex

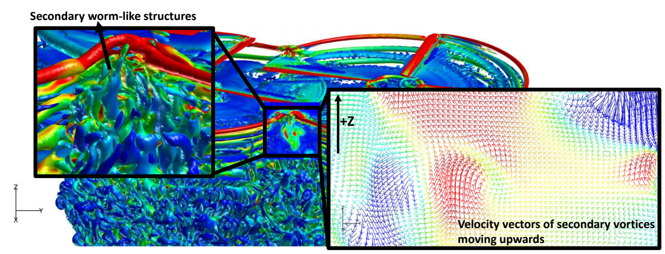

(c) Small secondary worm-like structures moving in the +Z direction

Fig. 10: Entrance and exit points of the overlap region for the 25% overlap case; Omega shaped vortex structure; small secondary worm-like structures.

Figure 12 shows a quantitative comparison of $dF_z/d\Psi$ of the right rotor for all rotor overlap configurations at the 75% span. Due to symmetry between the left and right rotor of the distribution of $dF_z/d\Psi$, only the right rotor is analyzed here. Once again, the results demonstrate that the magnitude of the BVI events located within 225° and 315° azimuths which is the range where the entrance and exit locations of the overlap region for all the rotor overlap configurations. The 25% overlap case shows significantly higher rotor-to-rotor BVI peaks located near 225° and 315° azimuths compared to the other overlap cases. It is anticipated that the 25% overlap configuration would result in the highest sound pressure level. In a later subsection, a relationship between the acoustic sources and the noise of the side-by-side rotor at a distinct observer location is studied.

It is useful to see the variation of the normal forces, especially in the overlap region, since the rate of the change in the normal force is the source of acoustics. Figures 13 and 14 show how the normal force is significantly affected by the increase in the overlap region. In Fig. 13, it compares the normal force for all overlap cases at different radial locations along the blade. It can be seen that the width, depth, and the rate of the change of the normal force significantly increase with

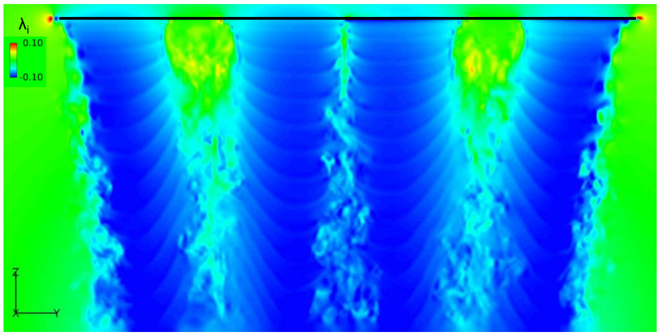

(a) 0% Overlap

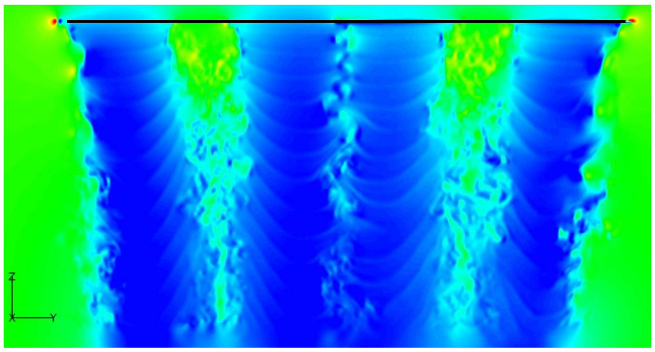

(b) 5% Overlap

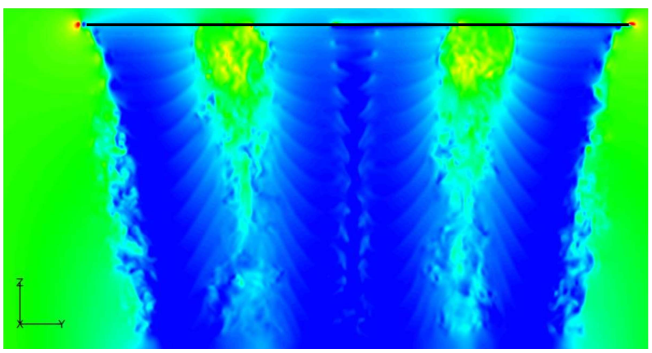

(c) 15% Overlap

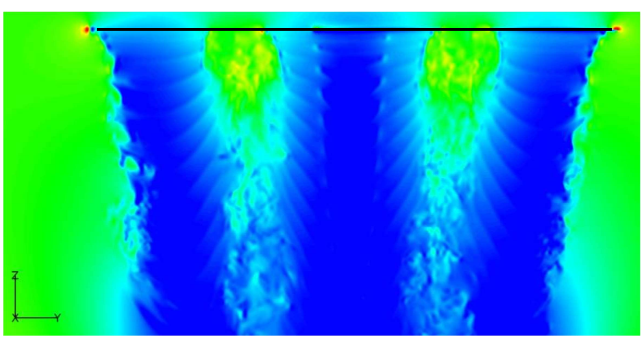

(d) 25% Overlap

Fig. 11: Comparison of λ_i (inflow ratio) between all of the overlap cases; the black bar represents the rotor disk plane.

increasing the overlap, especially for the 15% and 25% overlap configuration. Figure 14 shows the variation of the width and depth in the radial direction for each overlap case. As expected, the width of the overlap region increases with increasing the overlap percentage. We have added the 0% overlap as a reference since the width and depth of the normal force for this case do not necessarily represent the effect of the overlap. It is shown that the 5% overlap has similar width and depth as for the 0% overlap case, except near the tip. However, the 15% and 25% cases show large deviations from the 0% case. The significantly increased depth and the slope of the change will increase acoustics in the 15% and 25% overlap cases as will be shown later. The increased depth with a larger overlap may indicate the separation of acoustic pulses of each rotor blade. However, since we consider multiple blades as the noise source, the separation of acoustic pulses for one blade will not necessarily represent the total acoustic pressure pulse width, which will be discussed later.

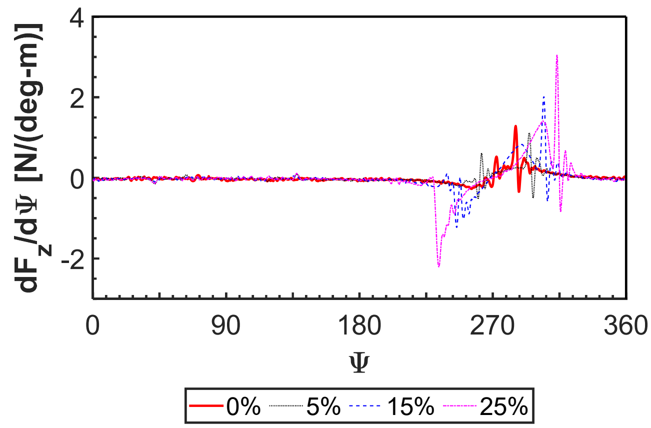

Fig. 12: Comparison of $dF_z/d\Psi$ of the right rotor at the 75% span

Effect of Rotor Overlap on Acoustics

Figure 15 shows that an increase in the rotor overlap increases the total acoustic pressure. The large and distinct acoustic peaks occur when the rotor blades either enter or exit the overlap region. The blade-vortex-interactions at these two locations are a direct correlation to the large acoustic peaks. However, there are also small variations between each of the peaks, which are mostly likely to be from the interaction of the rotor blades with the small secondary worm-like structures mentioned earlier. In Fig. 15, isolated rotor acoustic results are added as a reference since this isolated rotor does not exhibit rotor-to-rotor BVI. It is clearly seen that the acoustic pressure from the isolated rotor is almost negligible, which demonstrates the importance of the role of rotor-to-rotor BVI on the noise generation. Figure 16 show the contours of the first integrand of the loading noise portion as seen in Eq. (3), for the right rotor only due to symmetry. The black lines represent the rotor blades where at an observer time, at which the rotor blade enters or exits the overlap region. At the provided microphone positions, the key aerodynamic interactions that mostly affects the total acoustic pressure are:

- Rotor-to-rotor BVI events happening while entering (blue color) and exiting (red color) the overlap region for the 5%, 15%, and 25% overlap cases.

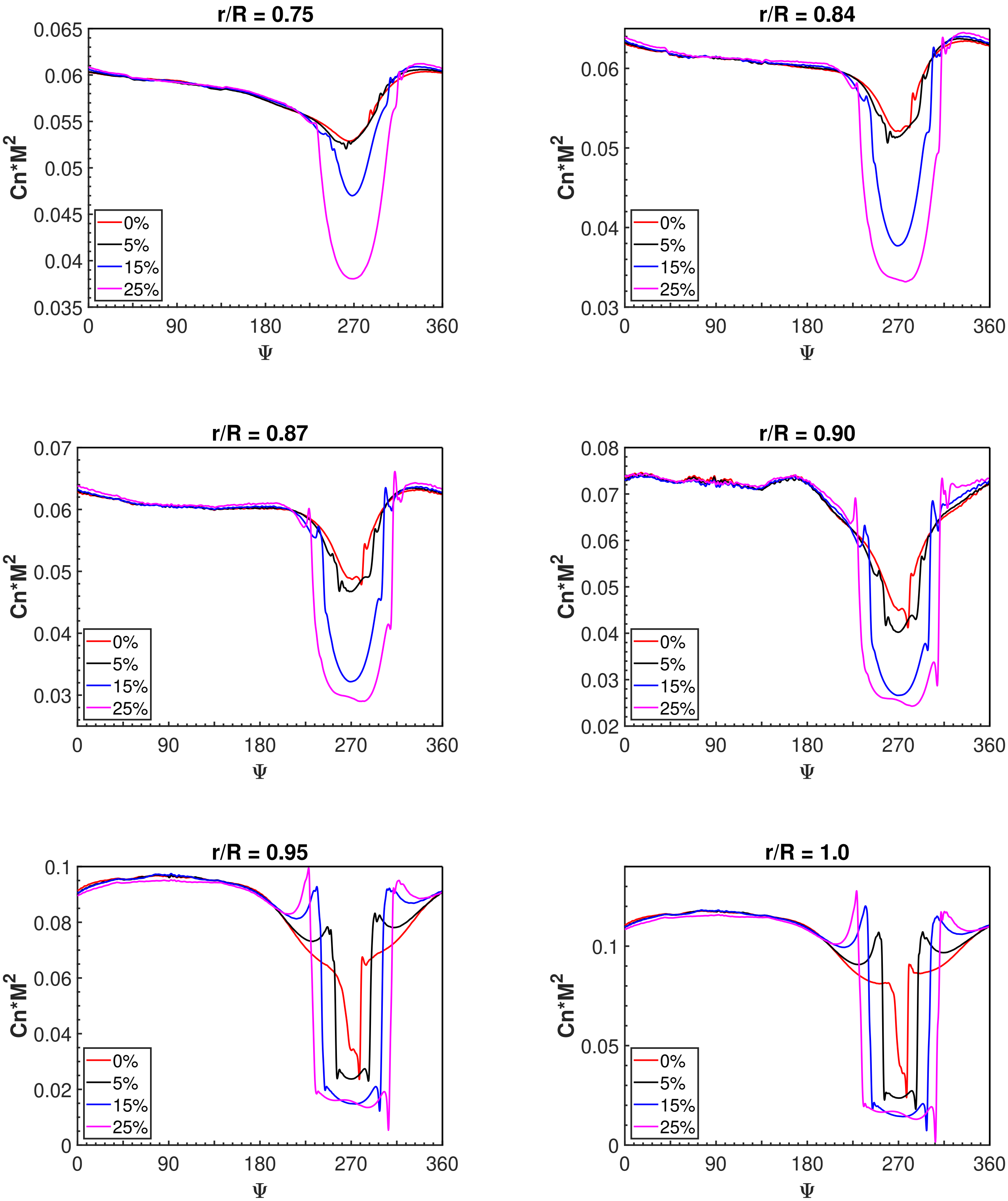

Fig. 13: The effect of rotor overlap for all of the overlap cases on normal force.

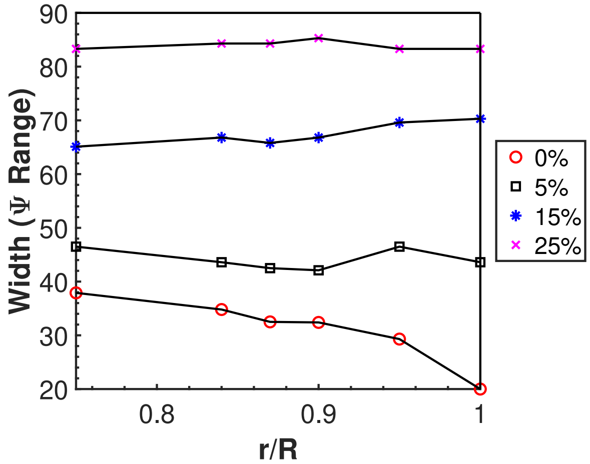

(a) Width

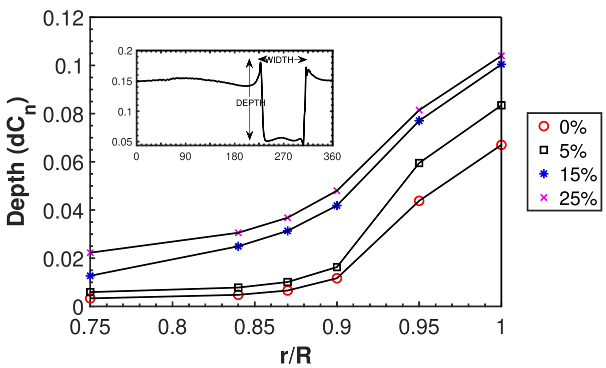

(b) Depth

Fig. 14: Overlap effect on the aerodynamic performance for all overlap cases

Looking at all the overlap cases, more notably the 25% overlap case, is significantly more impulsive in regard to the strength of the rotor-to-rotor BVI events.

In Fig. 17, blade 2 is coming out of the overlap region at the exit location just past the 270° azimuth (0% overlap) and about 315° azimuth (25% overlap) contributing to the large positive acoustic peaks at t = 0.1289 sec and t = 0.1389 sec respectively. In contrast, at t = 0.1242 sec and t = 0.1422 sec for the 0% overlap and 25% overlap cases respectively, blade 2 can be seen entering the overlap region, which contributes to the large negative acoustic peaks at the observer times. Figure 17 illustrates not only what is causing the large spike in the total acoustic pressure, but also the effect of blades on the acoustic peaks. For the 0% overlap, one blade contributes a pair of the negative and positive peaks at a relatively short time as it passes through the entrance and exit of the overlap. For the 25% overlap, a pair of the positive and negative peaks is contributed by two blades as one blade exits and the other blade enters the overlap region. The cause of the variations in the acoustic pressure between distinct peaks are likely due to the smaller secondary worm-like structures as it breaks down during the blade passage.

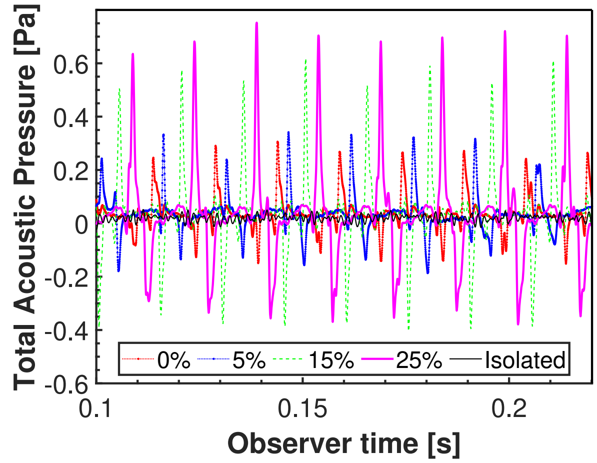

Fig. 15: Comparison of the total acoustic pressure of all rotor overlap cases and an isolated rotor case

Comparison with Background Noise Levels

As discussed in earlier sections, UAM aircraft noise can be one of the main barriers in gaining public acceptance especially if it exceeds background noise. As per guidelines from one of the largest promoters of UAM, Uber Technologies Inc., the UAM aircraft noise should be approximately 62 dB at an altitude of 500 ft (152.4 m), as well as needing to be 15 dB lower than that of a similar sized helicopter noise at the same altitude and flight operating conditions (Ref. 24). The acoustic results of the side-by-side rotor analyzed in this subsection are computed based on CFD simulations. Acoustic simulations are considered for all overlap cases in hover condition with a single observer positioned 500 ft (152.4 m) directly below the rotor disk plane. Figures 18 and 19 shows the one-third octave band sound pressure level (SPL) and overall sound pressure level (OASPL) respectively for each overlap case. Both plots show a comparison of each rotor overlap configuration to the background noise, which include freeway, community, park, and rural areas. Figure 19 clearly shows that all of the overlap cases exceed the Uber noise guideline of approximately 62 dB at an altitude of 500ft (152.4 m). It can be seen that the OASPL is lower for the 0% and 5% overlap cases by about 3.2 and 2.7 dB respectively compared to the freeway noise when operating at 500 ft (152.4 m), however, it exceeds the community, park, and rural noise. The same can be said for the one-third octave band SPL of the 0% and 5% overlap where, at lower frequencies, noise is lower than the freeway, rural, community, and park noise. However, there is a small range of frequency, which, for the same overlap configurations, exceeds the freeway background noise. The 15% and 25% overlap cases show as much as 20 dB larger than all background noise, especially in a 100-2,000 Hz frequency range. It should be noted that current calculations do not take into consideration a component of rotorcraft noise, broadband noise. As demonstrated in a previous study by Li and Lee (Refs. 25, 26), when multiple vehicles are operating simultaneously, UAM broadband noise could increase significantly, especially at high frequencies.

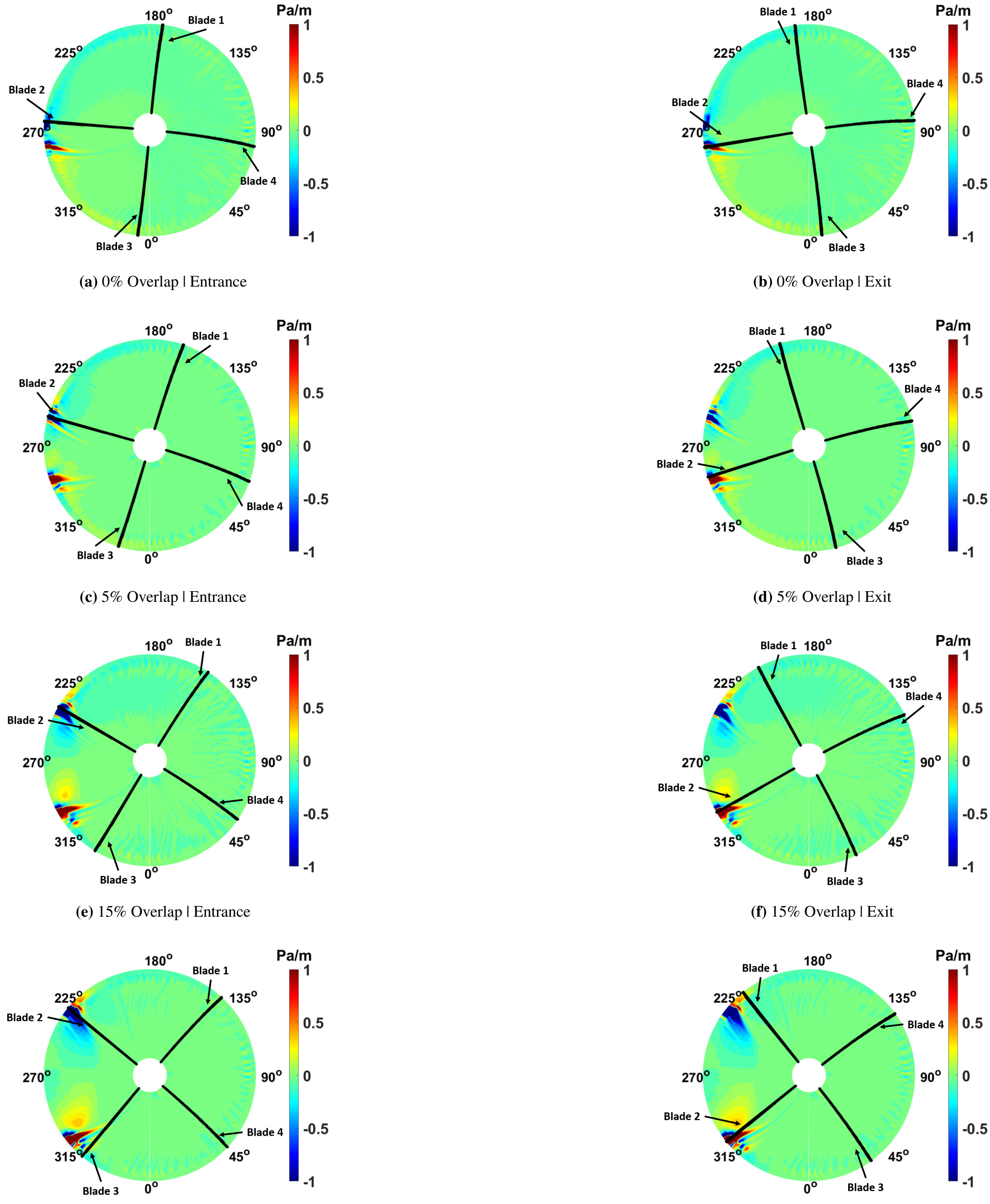

(a) 0% Overlap | Entrance

(b) 0% Overlap | Exit

(c) 5% Overlap | Entrance

(d) 5% Overlap | Exit

(e) 15% Overlap | Entrance

(f) 15% Overlap | Exit

(g) 25% Overlap | Entrance

(h) 25% Overlap | Exit

Fig. 16: Comparison of the noise integrand results of the right rotor for all of the rotor overlap cases.

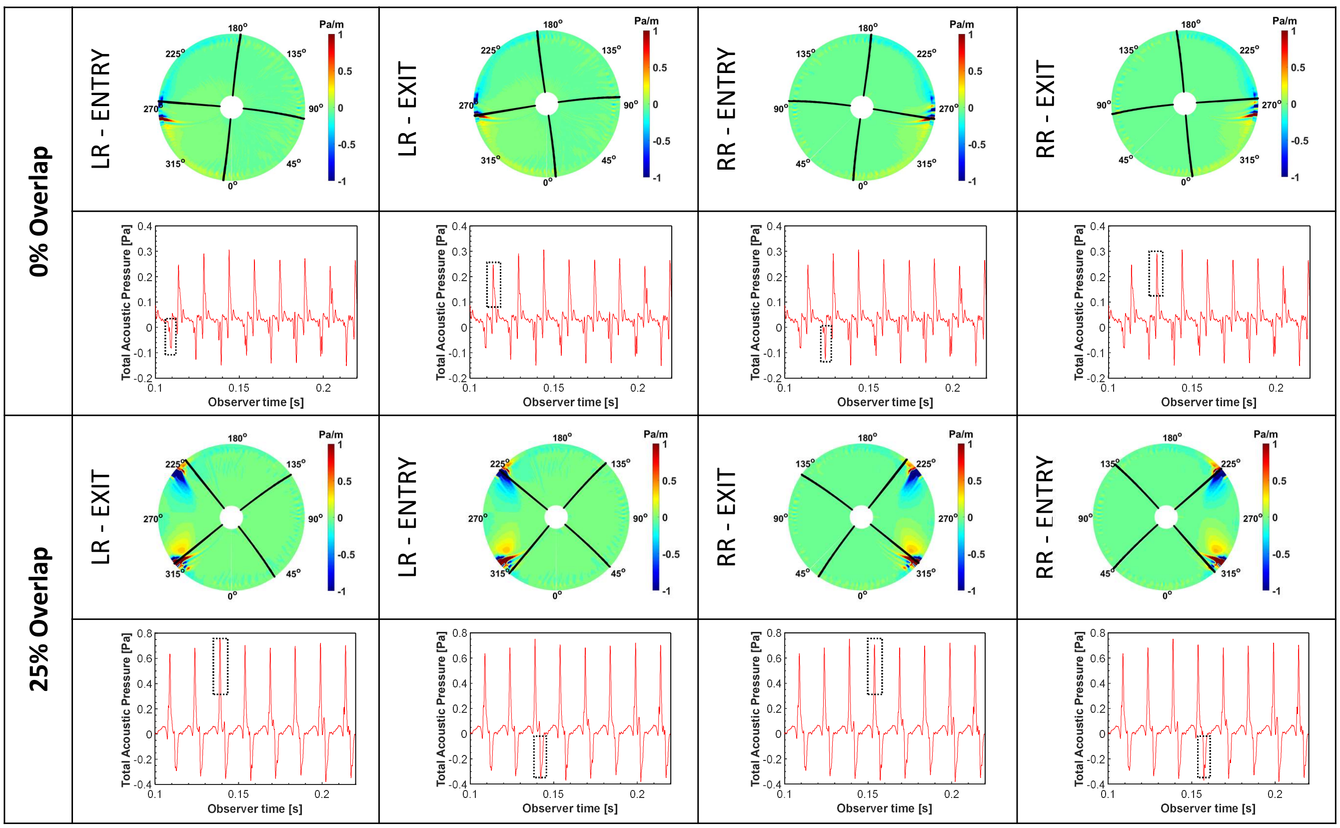

Fig. 17: Acoustic pressure as a function of observer time with entrance and exit locations visualizing the cause of the positive and negative peaks for both rotors (0% and 25% overlap case)

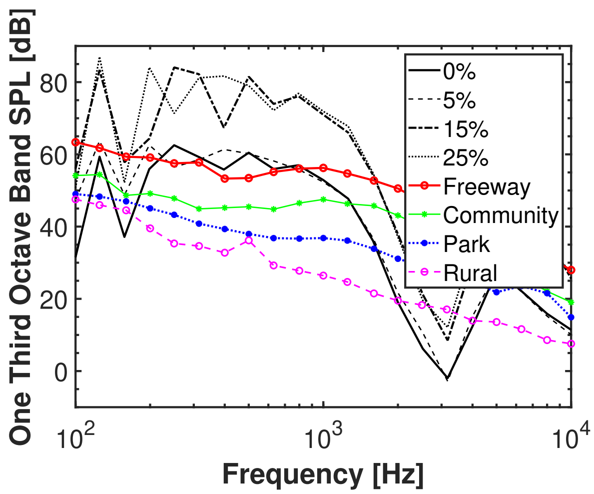

Fig. 18: Background noise comparison with each of the overlap cases in the one-third octave band SPL

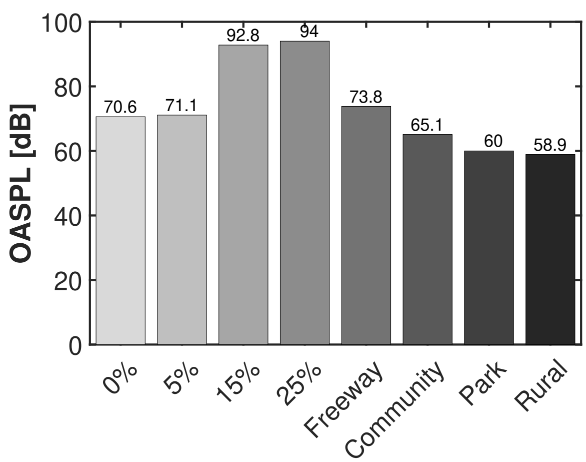

Fig. 19: OASPL of background noise comparison with each rotor overlap case

CONCLUSION

CFD simulations were performed using a high-fidelity tool, CREATE^{TM}-AV Helios, in order to study the acoustics of NASA's side-by-side rotor configuration with 0%, 5%, 15%, and 25% overlaps in the hover condition. Acoustic simulations based on an impermeable approach were carried out using PSU-WOPWOP, an acoustics prediction tool developed from Penn State. Detailed comparisons on the strength of the acoustic source for all rotor overlap configurations were performed. Connections between the different acoustic sources and the resulting noise were investigated for each overlap case. Comparisons between the side-by-side rotor noise and various background noise were also carried out in order to assess UAM aircraft noise as well as its impact on urban communities. Conclusions drawn based on the results presented and analyzed in this present work are the following:

1. The most dominant noise sources of the side-by-side rotor with rotor overlap in the hover condition are the blade-tip interactions with the tip vortical structures as the blade enters and exits the overlap region. These events are significantly stronger in magnitude than the self-BVI events for larger rotor overlap configurations (i.e. 25% overlap).

2. The 25% overlap case for the side-by-side rotor has a significantly higher noise level compared to the other overlap cases mainly due to substantial interactions between the blade and the vortical structures at the entrance and exit locations of the overlap region.

3. The noise guideline from Uber of 62 dB at an altitude of 500 ft (152.4 m) was not met for each rotor overlap configuration. Thus, technologies for noise reduction should be developed in order to improve the public acceptance for UAM operations.

4. The side-by-side rotor noise is not completely masked by various background noise at an altitude of 500 ft (152.4 m) in the hover condition. It is important to mention that broadband noise was not incorporated in the noise calculations of this paper. This signifies that the actual noise levels of the side-by-side rotor could possibly be higher. It is anticipated that, with multiple vehicles operating simultaneously, the noise level will even increase. Thus, it is important to pursue a way to reduce the impact of UAM aircraft noise, possibly with a way of optimizing the trajectory for all operating air vehicles including UAM or designing low-noise blades.

ACKNOWLEDGEMENTS

The authors would like to thank: Dr. Roger Strawn from the U.S. Army Capabilities Development Command Aviation and Missile Center (CCDC AvMC) | Technology Development Directorate (TDD-A) – NASA Ames Research Center and HPCMP for providing the DoD High Performance Computing (HPC) resources; Beatrice Roget and Rohit Jain from TDD-A for their astute advice and aid towards this research; Henry Jia from UC Davis for providing the meshes and OVERFLOW cases of the side-by-side rotor.

REFERENCES

[1]Silva, C., Johnson, W., Antcliff, K., and Patterson, M., "VTOL Urban Air Mobility Concept Vehicles for Technology Development," Paper AIAA 2018-3847, Aviation Technology, Integration, and Operations Conference, Indianapolis, IN, June 25–29, 2018.

[2]Moore, M., "21st Century Personal Air Vehicle Research," Paper GA-9, AIAA International Air and Space Symposium and Exposition, Dayton, OH, July 14–17, 2003.

[3]Johnson, W., Silva, C., and Eduardo, S., "Concept Vehicles for VTOL Air Taxi Operations," AHS Technical Conference on Aeromechanics Design for Transformative Vertical Flight, San Francisco, CA, January 16–19, 2019.

[4]Holden, J. and Goel, N., "Fast-Forwarding to a Future of On-Demand Urban Air Transportation," Uber Elevate, October 27, 2016.

[5]Johnson, W. and Silva, C., "Observations from Exploration of VTOL Urban Air Mobility Designs," Moffett Field, CA, June 2, 2018.

[6]Johnson, W. and Silva, C., "Observations from Exploration of VTOL Urban Air Mobility Designs," 7th Asian/Australian Rotorcraft Forum, Jeju Island, South Korea, October–November 30–1, 2018.

[7]Diaz, P., Johnson, W., Ahmad, J., and Yoon, S., "The Side-by-Side Urban Air Taxi Concept," Paper AIAA 2019-2828, AIAA Aviation Forum, Dallas, TX, June 17–21, 2019.

[8]Diaz, P. and Yoon, S., "High-Fidelity Computational Aerodynamics of Multi-Rotor Unmanned Aerial Vehicles," Paper AIAA 2018-1266, 56th AIAA Science and Technology Forum and Exposition, Kissimmee, FL, January 8–12, 2018.

[9]Nichols, R. and Buning, P., *User's Manual for OVERFLOW 2.1*, 2008, pp. B1–B16.

[10]Jia, Z. and Lee, S., "Acoustic Analysis of a Quadrotor eVTOL Design via High-Fidelity Simulations," Paper AIAA 2019-2631, 25th AIAA/CEAS Aeroacoustics Conference, Deflt, Netherlands, May 20–23, 2019.

[11]Jia, Z. and Lee, S., "Aeroacoustic Analysis of a Side-by-Side Hybrid VTOL Aircraft," 76th VFS International Annual Forum, Virtual Event, October 5–8, 2020.

[12]Jia, Z. and Lee, S., "Acoustic Analysis of Urban Air Mobility Quadrotor Aircraft," VFS Aeromechanics for Advanced Vertical Flight Technical Meeting, San Jose, CA, January 20–23, 2020.

[13]Sagaga, J. and Lee, S., "Simulations of Ducted and Coaxial Rotors for Air Taxi Operations," Paper AIAA 2020-2795, AIAA Aviation Forum, Virtual Event, June 15–19, 2020.

[14]Sitaraman, J., Jayaraman, B., Datta, A., Potsdam, M., Wissink, A. M., Jain, R., Adamec, S., and Abras, J., *Helios User Guide V.8.0*, HPCMP CREATE™, 2018, pp. 67–122.

[15]Lee, S., Bretner, K., Farassat, F., and Morris, P. J., "Analytic formulation and numerical implementation of an acoustic pressure gradient prediction," *Journal of Sound and Vibration*, Vol. 319, (3–5), 2009, pp. 1200–1221.

[16]Brentner, K. S., Brés, G. A., Perez, G., and Jones, H. E., "Maneuvering Rotorcraft Noise Prediction: A New Code for a New Problem," Proceedings of the American Helicopter Society Aerodynamics, Acoustics, and Test and Evaluation Technical Specialist Meeting, San Francisco, CA, January 13–25, 2002.

[17]Bretner, K. and Farassat, F., "Modeling aerodynamically generated sound of helicopter rotors," *Progress in Aerospace Sciences*, Vol. 39, (2–3), 2003, pp. 83–120.

[18]Brentner, K. S. and Jones, H. E., "Noise Prediction for Maneuvering Rotorcraft," Paper AIAA 2000-2013, 6th AIAA/CEAS Aeroacoustics Conference, Lahaina, HI, June 12–14, 2000.

[19]Ffowcs, W. and Hawkings, D. L., "Sound generation by turbulence and surfaces in arbitrary motion," *Philosophical Transactions of the Royal Society of London. Series A, Mathematical and Physical Sciences*, Vol. 264, (1151), 1969, pp. 321–342.

[20]Bodling, A. and Potsdam, M., "Numerical Investigation of Secondary Vortex Structures in a Rotor Wake," 76th VFS International Annual Forum, Virtual Event, October 5–8, 2020.

[21]Abras, J., Hariharan, N. S., and Narducci, R. P., "Wake Breakdown of High fidelity Simulations of a Rotor in Hover," 57th AIAA AIAA Science and Technology Forum and Exposition, San Diego, CA, January 7–11, 2019.

[22]Hariharan, N. S., Abras, J., and Narducci, R. P., "An Overview of Wake Breakdown in High-Fidelity Simulations ofRotor-in-Hover," 76th VFS International Annual Forum, Virtual Event, October 5–8, 2020.

[23]Abras, J., Narducci, R. P., and Hariharan, N. S., "Impact of High-Fidelity Simulation Variations on Wake Breakdown ofa Rotor in Hover," 58th AIAA AIAA Science and Technology Forum and Exposition, Orlando, FL, January 7–11, 2020.

[24]Carpenter, P. J. and Friedovich, B., "Effect of a Rapid Blade-Pitch Increase on the Thrust and Induced-Velocity Response of a Full-Scale Helicopter Rotor," NACA TN 3044, 1953.

[25]Li, S. and Lee, S., "Prediction of Rotorcraft Broadband Trailing-Edge Noise and Parameter Sensitivity Study," *Journal of the American Helicopter Society*, Vol. 65, (4), 2020, pp. 1–14(14).

[26]Li, S. and Lee, S., "UCD-QuietFly: A New Program to Predict Multi-Rotor eVTOL Broadband Noise," VFS Aeromechanics for Advanced Flight Technical Meeting, San Jose, CA, January 20–23, 2020.